October, 2016

Cell-autonomous regulation of dendritic spine density by PirB.

Dr. George S. Vidal, *James Madison University*
Maja Djurisic
Kiana Brown
Richard W Sapp
Carla J Shatz

eNeuro

Research Article: New Research | Development

Cell-autonomous regulation of dendritic spine density by PirB

Spines and excitatory synapses coregulated by PirB

George S. Vidal*, Maja Djurisic*, Kiana Brown, Richard W. Sapp and Carla J. Shatz

Departments of Biology and Neurobiology, and Bio-X, James H. Clark Center, Stanford University, Stanford, California, 94305.

DOI: 10.1523/ENEURO.0089-16.2016

Received: 19 April 2016

Revised: 17 September 2016

Accepted: 23 September 2016

Published: 28 September 2016

Author contributions: G.S.V., M.D., and C.J.S. designed research; G.S.V., M.D., K.B., and R.W.S. performed research; G.S.V. and K.B. analyzed data; G.S.V., M.D. and C.J.S. wrote the paper.

Funding: National Eye Institute: EY002858. G Harold and Leila Y. Mathers Foundation: 100001229. Regina Casper Stanford Graduate Fellowship; National Eye Institute: EY023518. Stanford Bio-X Undergraduate Research Fellowship; Stanford Bio-X Undergraduate Research Fellowship;

Authors report no competing financial interests.

National Eye Institute R01 grant EY002858 and the G. Harold and Leila Y. Mathers Charitable Foundation to C.J.S., Regina Casper Stanford Graduate Fellowship and National Eye Institute F31 grant EY023518 to G.S.V., Stanford Bio-X Undergraduate Summer Research Fellowships to K.B. and R.W.S.

*These authors contributed equally to this work.

Correspondence should be addressed to either Carla J. Shatz, James H. Clark Center, 318 Campus Drive W1.1, Stanford, California 94305. Email: cshatz@stanford.edu, or George S. Vidal, Email: vidalgx@jmu.edu

Cite as: eNeuro 2016; 10.1523/ENEURO.0089-16.2016

Manuscript title: Cell-autonomous regulation of dendritic spine density by PirB

Abbreviated title (50-character limit): Spines and excitatory synapses coregulated by PirB

Authors and affiliations:
George S. Vidal[1,2*], Maja Djurisic[1*], Kiana Brown[1], Richard W. Sapp[1], and Carla J. Shatz[1]
[1]Departments of Biology and Neurobiology, and Bio-X, James H. Clark Center, Stanford University, Stanford, California, 94305.
[2]Current address: Department of Biology, James Madison University, MSC 7801, Harrisonburg, Virginia, 22807
[*]These authors contributed equally to this work.

Author contributions: G.S.V., M.D., and C.J.S. designed research; G.S.V., M.D., K.B., and R.W.S. performed research; G.S.V. and K.B. analyzed data; G.S.V., M.D. and C.J.S. wrote the paper.

Correspondence should be addressed to: Carla J. Shatz, James H. Clark Center, 318 Campus Drive W1.1, Stanford, California 94305. Email: cshatz@stanford.edu, and to George S. Vidal, Email: vidalgx@jmu.edu

Number of figures: 6
Number of tables: 1
Number of multimedia: 0
Number of words for Abstract: 254
Number of words for Significance: 125
Number of words for Introduction: 724
Number of words for Discussion: 1201

Acknowledgements: We thank P. Kemper, C. Chechelski, and N. Sotelo-Kury for excellent mouse husbandry, we thank Drs. B. Brott and K. Chew for helpful discussions, and we thank Drs. K. Srinivasan, S. K. McConnell, H. Lee, and G. Panagiotakos for assistance with the *in utero* electroporation method.

Conflict of interest: Authors report no competing financial interests.

Funding sources: National Eye Institute R01 grant EY002858 and the G. Harold and Leila Y. Mathers Charitable Foundation to C.J.S., Regina Casper Stanford Graduate Fellowship and National Eye Institute F31 grant EY023518 to G.S.V., Stanford Bio-X Undergraduate Summer Research Fellowships to K.B. and R.W.S.

ABSTRACT

Synapse density on cortical pyramidal neurons is modulated by experience. This process is highest during developmental critical periods, when mechanisms of synaptic plasticity are fully engaged. In mouse visual cortex, the critical period for ocular dominance (OD) plasticity coincides with developmental pruning of synapses. At this time, mice lacking Paired immunoglobulin-like receptor B (PirB) have excess numbers of dendritic spines on L5 neurons; these spines persist and are thought to underlie the juvenile-like OD plasticity observed in adulthood. Here we examine if PirB is required specifically in excitatory neurons to exert its effect on dendritic spine and synapse density during the critical period. In mice with a conditional allele of PirB ($PirB^{fl/fl}$), PirB was deleted only from L2/3 cortical pyramidal neurons *in vivo* by timed *in utero* electroporation of Cre recombinase. Sparse mosaic expression of Cre produced neurons lacking PirB in a sea of wild-type neurons and glia. These neurons had significantly elevated dendritic spine density, as well as increased frequency of miniature excitatory postsynaptic currents (mEPSCs), suggesting that they receive a greater number of synaptic inputs relative to Cre– neighbors. The effect of cell-specific PirB deletion on dendritic spine density was not accompanied by changes in dendritic branching complexity or axonal bouton density. Together, results imply a neuron-specific, cell-autonomous action of PirB on synaptic density in L2/3 pyramidal cells of visual cortex. Moreover, they are consistent with the idea that PirB functions normally to co-repress spine density and synaptic plasticity, thereby maintaining headroom for cells to encode ongoing experience-dependent structural change throughout life.

SIGNIFICANCE STATEMENT

Dendritic spines, postsynaptic sites of excitatory synapses on pyramidal neurons, are regulated by experience and synaptic plasticity. Paired immunoglobulin receptor B (PirB) is known to restrict the extent of experience-dependent plasticity in visual cortex. Here we report that when PirB is removed *in vivo* from just a few isolated pyramidal neurons in layer 2/3 of mouse visual cortex, spine density as well as the frequency of miniature synaptic currents (a measure of the density of functional synapses) are elevated selectively in the cells lacking PirB. These results suggest that PirB expression in individual neurons is sufficient to limit excitatory synaptic density on pyramidal neurons. This cell intrinsic function of PirB could serve to ensure that pyramidal cells have sufficient structural reserve to encode new experiences.

INTRODUCTION

Cortical circuits are altered by experience throughout life and undergo extensive restructuring during early developmental critical periods. Underlying these experience-dependent circuit changes are cellular and molecular mechanisms of synaptic plasticity. Different learning and plasticity paradigms involving specific cortical regions result in a persistent increase in the density of dendritic spines, which are postsynaptic anatomical structures at excitatory synapses and represent sites of plasticity. This increase in dendritic spine density is thought to represent a structural trace of new learning. For example, mice trained on a forepaw reaching task show an increase in dendritic spine density on apical dendrites of L5 pyramidal cells in motor cortex (Xu *et al*., 2009b; Fu *et al*., 2012); changes are also seen in spine density on the dendrites of L2/3 pyramidal cells (Ma *et al.*, 2016). When these newly formed spines are selectively disassembled,

86 motor memories are erased (Hayashi-Takagi *et al*., 2015). In the binocular zone of mouse visual
87 cortex, closure of one eye (monocular deprivation) generates an experience-dependent form of
88 plasticity known as ocular dominance (OD) plasticity (Gordon and Stryker, 1996). This plasticity
89 is accompanied by an enduring increase in spine density along the apical tufts of L5 pyramidal
90 neurons (Hofer *et al.*, 2009; Djurisic *et al.*, 2013). As in motor cortex, this net increase in density
91 is thought to provide a structural substrate that mediates a lower threshold for OD plasticity
92 when the same eye is closed again later in life (Hofer *et al.,* 2006; Hofer *et al.*, 2009).
93 In recent years, a list of molecules that appear to function normally as *negative* regulators
94 of visual cortical plasticity has emerged, in the sense that gene knockout *enhances* OD plasticity
95 following brief monocular deprivation. Blockade, removal, or genetic deletion of each of these
96 molecules, including NgR1 (Nogo Receptor 1; McGee *et al.*, 2005; Frantz *et al.*, 2016), Lynx1
97 (Morishita *et al.*, 2010; Bukhari *et al*., 2015), DR6 (Death Receptor 6; Marik *et al.*, 2013),
98 CSPGs (Chondroitin sulfate proteoglycans; Pizzorusso *et al*., 2002), or PirB (Paired
99 immunoglobulin-like receptor B, Syken *et al.,* 2006; Djurisic *et al*., 2013; Bochner *et al*., 2014)
100 generates enhanced OD plasticity even in adult mice, well after normal closure of the critical
101 period and when significant OD plasticity cannot be elicited in wild-type mice. In addition, cell
102 type specific deletion of PirB from excitatory pyramidal neurons is sufficient to generate
103 enhanced OD plasticity in adult visual cortex (Bochner et al, 2014). In mice with germline
104 deletion ($PirB^{-/-}$), dendritic spine density is elevated not only during the critical period but also
105 in adult, implying a developmental pruning defect (Djurisic *et al.*, 2013). This elevation in spine
106 density is thought to mediate the juvenile-like OD plasticity observed in adult visual cortex of
107 these mice.

PirB is expressed in cortical pyramidal neurons. It was discovered in an *in situ* hybridization screen designed to identify receptors expressed in brain that bind MHC class I molecules, which are involved in activity-dependent plasticity (Syken et al, 2006; Adelson *et al.*, 2012; Djurisic *et al.*, 2013; Bochner *et al*., 2014). The elevated spine density and enhanced OD plasticity in visual cortex of $PirB^{-/-}$ mice could arise from a requirement for PirB function exclusively in neurons. Microglia are also intimately involved in synapse pruning (Schafer *et al.*, 2012, Parkhurst *et al.*, 2013), but PirB expression has not been detected in this cell type *in vivo*. Nevertheless, studies of germline PirB knockout mice, in which both brain and immune systems are affected, cannot distinguish between these alternatives. Here we use timed *in utero* electroporation of Cre recombinase into developing $PirB^{fl/fl}$ mouse ventricular zone (Saito and Nakatsuji, 2001) to investigate if neuron-specific deletion of PirB is sufficient to explain changes in dendritic spine density seen in germline $PirB^{-/-}$ (Djurisic *et al.*, 2013) or following pharmacological blockade of PirB in adult wild type visual cortex (Bochner et al, 2014). In addition, *in utero* electroporation permits sparse deletion of PirB in single L2/3 neurons embedded in a wild type environment. This type of mosaic approach has been used *in vivo* to determine if a particular gene function is cell autonomous (Hippenmeyer *et al.*, 2010; Akbik et al., 2013; Lu *et al.*, 2013). Here, sparse deletion of PirB in L2/3 pyramidal neurons demonstrates that neuronal PirB is required for regulation of synaptic density, leading us to conclude that this function of PirB is cell intrinsic.

MATERIALS AND METHODS

Mice. $PirB^{fl/fl}$, $PirB^{+/+}$, and $PirB^{-/-}$ were generated by Syken et al. (2006). Briefly, $PirB^{fl/fl}$ mice were generated by electroporating a construct with loxP sites flanking exons 10-13 of PirB into the 129 J1 ES line derived from agouti 129S4/SvJae mice. Exons 10-13 of PirB code for the transmembrane domain of PirB, as well as part of the intracellular domain encompassing the signaling immunoreceptor tyrosine-based inhibitory motifs (ITIMs). Thus, Cre-mediated excision of exons 10-13 from the PirB gene in $PirB^{fl/fl}$ mice results in a truncated protein that is unable to signal, as shown previously by anti-phosphotyrosine immunoprecipitation experiments (Syken et al., 2006). To generate mice with germ line deletion of PirB ($PirB^{-/-}$), a deleter strain that targets Cre-recombinase expression to early mouse embryo via adenovirus EIIa promoter (B6.FVB-TGN(EIIa-cre)C5379Lmgd, Jakcson) was crossed to $PirB^{fl/fl}$ mice. Heterozygote sibling matings were then used to generate both control $PirB^{+/+}$ line and a homozygous $PirB^{-/-}$ line (Syken et al., 2006). $PirB^{fl/fl}$, $PirB^{+/+}$, and $PirB^{-/-}$ were maintained as three separate lines on the same mixed genetic background (C57BL/6 x SV/129J). Previous studies have shown that excision of PirB from $PirB^{fl/fl}$ by Cre recombinase under control of the UbC promoter occurs within one week (Bochner et al., 2014), and is accompanied by a complete loss of PirB protein after about 3 weeks from the onset of Cre recombinase expression (e.g. Figure 1, Bochner *et al.*, 2014). Cre recombinase expression via the GFP.Cre construct under the PGK (phosphoglycerate kinase) promoter used here for the electroporation experiments described below should be even more rapid and efficient (Qin *et al*., 2010).

All experiments were carried out in accordance with the Guide for the Care and Use of Laboratory Animals of the National Institutes of Health and approved by the [Author University] Institutional Animal Care and Use Committee. Experimental methods are also in accordance

with the Policies of the Society for Neuroscience on the Use of Animals and Humans in Neuroscience Research. All mice were maintained in a pathogen-free environment.

In utero electroporation. Female mice were mated within the same line ($PirB^{+/+}$, $PirB^{fl/fl}$, or $PirB^{-/-}$) and checked daily for vaginal plugs. The day that a plug was found was counted as embryonic day 0.5 (E0.5). *In utero* electroporation was performed at embryonic day 15.5, when L2/3 cortical neurons are generated (Tabata and Nakajima, 2001; Saito and Nakatsuji, 2001; Saito, 2006; Chen *et al.*, 2008). Pregnant mice were anaesthetized using 1% - 2.5% isofluorane in 100% O_2. Using sterile surgical technique, a midline incision was made to the abdominal wall to expose the uterine horns. Lateral ventricles of embryos were injected with either 1.0 or 1.5 µl of 1.9-2.0 µg/µl GFP.Cre in Tris-EDTA buffer (10mM Tris-HCl, pH 8.0, and 1mM ethylenediaminetetraacetic acid); injection of the lower (1.0 µl) volume of DNA was critical to achieving sparse electroporations.

The GFP.Cre is an expression construct in which GFP expression is driven by the ubiquitin C promoter, and Cre expression is driven separately by the phosphoglycerate kinase promoter (gift from Tyler Jacks, Addgene plasmid #20781; Scotto-Lomassese *et al.,* 2011; Andreu-Agullo *et al.,* 2011). Injections were achieved using micropipettes made from glass capillary tubes (TW100F-4, World Precision Instruments, Inc.) pulled into a fine tip with a micropipette puller (P-97, Sutter Instruments). Tweezer-type circular electrodes (5 mm in diameter) were custom made by coiling 24 AWG platinum wire (PTP201, World Precision Instruments Inc.) and were used to deliver five 50-ms electric pulses at 45 V with 950 ms intervals, using a square-wave generator (ECM 830, BTX). The exposed uterus was kept moist with 0.9% saline at 37 °C. After each electroporation procedure, dams were given buprenorphine intraperitoneally (0.1 mg/kg, cat. #2808, Tocris), the abdominal wall was sutured shut, and the

dam was allowed to recover in a cage kept at around 37°C. Pregnant dams were monitored postoperatively until after giving birth and able to nurse pups.

Histology: Mice received an overdose of sodium pentobarbital (>86 mg/kg) and sodium phenytoin cocktail (Beuthanasia-D, Merck; >11 mg/kg) intraperitoneally, and brain tissue was fixed via transcardial perfusion of ice-cold 0.1M sodium phosphate-buffered saline (PBS) followed by ice-cold 4% (wt/vol) paraformaldehyde in 0.1 M PBS. Brains were then post-fixed overnight in 4% (wt/vol) paraformaldehyde in PBS at 4ºC, followed by 12-24 h in PBS at 4ºC. Brains were cut coronally using a vibrating microtome (VT1200S, Leica Microsystems) into 150 µm-thick sections. Sections were mounted on Superfrost Plus glass slides (VWR) with ProLong Gold antifade reagent (Invitrogen Corp.) as a mounting medium and covered with #1.5-thickness cover glass (VWR).

Dendritic spine and axonal bouton imaging and analysis: Slides of histological sections prepared as described above were initially screened for GFP fluorescence using low-powered objectives on an Eclipse E800 microscope (Nikon Corporation), without knowledge of genotype. GFP-positive neurons in L2/3 of visual cortex were then identified by comparing landmarks observed via DAPI fluorescence and brightfield imaging (Eclipse E800 microscope), including the shape of the internal capsule, the hippocampus, thalamic structures, and cytoarchitectonic differences between the cortical layers (Paxinos and Franklin, 2008). Labeled cells with low expression levels of GFP and without complete primary dendritic arbors were excluded from further imaging. High-resolution images of apical and basal dendrites of L2/3 pyramidal neurons in visual cortex, and of continuous 100-300 µm segments of descending axons in L5, were taken on an SP2 or SP8 confocal microscope (Leica Microsystems), or on a two-photon microscope (Prairie Technologies); 63x/1.40 NA oil-immersion (Leica) or 60x/1.1 NA water-immersion

(Prairie) objectives were used. Images were acquired at or over the theoretical Nyquist sampling rate for each objective used (~71nm/px). All dendritic spine and axonal bouton analysis was performed manually while blind to genotype using ImageJ software (National Institutes of Health); manual tracing with ImageJ Simple Neurite Tracer plugin was used for length measurement of neurites. Axonal boutons were identified as in De Paola *et al.*, 2006.

Sholl analysis: Images acquired by two-photon microscopy using 10 × or 40 × objectives (Prairie) that contained the entire L2/3 neuron dendritic arbor in a 150 µm thick section were used for Sholl analysis (Sholl, 1953). For each cell, concentric circles were drawn at 10, 30, 50, 70, 90, 110, and 130 µm from the geometric center of the soma (0 µm), using the Concentric Circles ImageJ plugin. The number of crossings of dendritic branches belonging to individual cells through each circle were counted, and used as the measure of the complexity of the dendritic arbor.

Assessment of neuronal labeling density resulting from electroporations: Low-magnification images of L2/3 GFP+;Cre+ $PirB^{fl/fl}$ neurons were acquired (Eclipse E800 microscope) that included all GFP+ neurons within a 0.5 mm radius of a GFP+ neuron of interest. For each cell, concentric circles were drawn at 50 µm intervals from the geometric center of the soma (0 µm), using the Concentric Circles ImageJ plugin. The number of GFP+ cells located within each ring (e.g. 50 µm -100 µm) was then counted to derive a density vs. distance measurement of distribution of the electroporated neighboring cells surrounding a neuron of interest (e.g. Figure 2F).

Electrophysiology: At P28-32, $PirB^{+/+}$ and $PirB^{fl/fl}$ mice that had been electroporated *in utero* at E15.5 were overdosed with an intra-peritoneal injection of ketamine (132 mg/kg; Phoenix), xylazine (14 mg/kg; Akorn), acepromazine (0.2 mg/kg; Boehringer Ingelheim)

cocktail; after deep anesthesia, mice were decapitated. Brains were immediately removed and immersed in N-methyl D-glucamine (NMDG)-based ice-cold slicing buffer, to minimize damage from excitotoxicity and hypoxia (composition: 135 mM NMDG, 1 mM KCl, 1.2 mM KH_2PO_4, 1.5 mM $MgCl_2$, 0.5 mM $CaCl_2$, 20 mM choline bicarbonate, and 10 mM glucose, pH 7.4, equilibrated with 95% O_2 and 5% CO_2. Brains were cut coronally at 400 μm, using a vibrating microtome (VT1000S, Leica Microsystems). Sections were transferred to a recovery chamber containing high-magnesium artificial cerebrospinal fluid (ACSF). (ACSF composition: 125 mM NaCl, 26 mM $NaHCO_3$, 2.3 mM KCl, 1.26 mM KH_2PO_4, 4.0 mM $MgCl_2$, 2.5 mM $CaCl_2$, and 20 mM glucose, pH 7.4, equilibrated with 95% O_2 and 5% CO_2) Slices recovered at 37 °C for 30 min, and an additional 30 min at room temperature before recording (Crozier *et al.*, 2007; Djurisic et al., 2013).

The whole-cell patch-clamp technique was used to record miniature excitatory postsynaptic currents (mEPSCs) from individual pyramidal cells in slices containing primary visual cortex and binocular zone. Single, GFP-labeled or unlabeled L2/3 pyramidal neurons in visual cortex were visualized using infrared differential interference contrast (IR-DIC) illumination combined with fluorescent illumination in an Olympus BX51WI microscope via a 60 × water immersion objective coupled with an additional 2 × zoom lens (120 × final magnification). For GFP negative cells, only those with pyramidal-shaped somata and a visible apical dendrite oriented perpendicular to the pial surface were selected for recordings. External bath solution (ACSF) was maintained at ~30 °C, and bubbled with 95% O_2 / 5% CO_2 for the duration of the experiment. Patch-clamp electrodes 1.5 – 4.2 MΩ, were filled with cesium-based intracellular solution (composition: 135 mM CsCl, 10 mM Hepes, 1 mM EGTA, 4 mM Mg-ATP, 0.4 mM Na-GTP, pH 7.4 with NaOH). To reveal the morphology of neurons from which

mEPSCs were recorded, biocytin (cat. #B4261, Sigma) was added to the intracellular solution at a final concentration of 5 mg/ml; after recording, sections were fixed in 4% paraformaldehyde overnight, followed by permeabilization and staining with Texas Red – conjugated avidin (cat. #A-2006, Vector Laboratories, Burlingame, California; 1:10). Once in whole-cell mode, the pipette solution equilibrated with the cell contents for 5 – 10 min before recording. Miniature excitatory postsynaptic AMPA currents were isolated pharmacologically using 1 μM TTX (tetrodotoxin, cat. #1078, Tocris Bioscience, Bristol, United Kingdom), 50 μM AP-5 (DL-2-Amino-5-phosphonopentanoic acid; cat. #A5282, Sigma Aldrich, St. Louis, Missouri), and 10 μM gabazine (SR95531; cat. #1262, Tocris). Series resistance was 9 – 20 MΩ. A low-noise AxoPatch 200B patch-clamp amplifier, DigiData 1322A digitizer, and Clampex software (Molecular Devices, Sunnyvale, California) were used for data collection. Before analysis, recordings across all conditions were filtered with a 60 Hz, 3-harmonic, 100-cycle electrical interference filter (Molecular Devices), as well as a Gaussian, 53-coefficient low-pass filter, setting the -3dB to 2 kHz (Molecular Devices). Analysis of mEPSCs was done using MiniAnalysis software, ver. 6.0.7 (Synaptosoft), and performed blind both to genotype and to cell identity (*i.e.* GFP+ vs. GFP–). Cells with cell capacitance of 60 pF and/or leak current more negative than -150 pA were excluded from the analysis. Root mean square (RMS) baseline noise was calculated from three different places during the 10 minute recording, and was less than 3 pA. Automatic detection parameters in MiniAnalysis were adapted from Xu et al., 2009a and Muhia et al., 2012, and were as follows: threshold was set to 4 times the RMS noise value, period to search for a local maximum was 20 ms, time before peak to establish baseline was 5 ms, period to search a decay time was 5 ms, fraction of peak to find a decay time was 0.5, period to average baseline was 2 ms, area threshold was 5 times the RMS noise value, and number of

points to average to establish peak was 3. Continuous automatic analysis was run during 1 to 2 minutes of the 10-minute recording in which the leak current was most stable; detected events were manually inspected to eliminate false positives.

Statistics. All statistical analyses and graphs were done with GraphPad Prism software, and power analyses were done using G*Power software (Heinrich-Heine-Universität Düsseldorf; http://www.gpower.hhu.de/; Faul *et al*., 2007, 2009). Data are presented as mean ± SEM; sample size (n) is the number of cells analyzed, followed by the number of mice used for the entire sample, unless noted otherwise in the text. Analyses were performed blind to genotype and condition.

Table 1: Statistical table

	Data structure	Type of test	Power (alpha=0.05)	p-value
a (Figure 1I and 2G)	normality assumed (Levene's test p=0.118)	One-Way ANOVA with Bonferroni's multiple comparisons post-hoc test	0.9403	$PirB^{+/+}$ Cre^{+} vs. $PirB^{-/-}$ Cre^{+} p=0.004; $PirB^{+/+}$ Cre^{+} vs. $PirB^{fl/fl}$ Cre^{+} p=0.041; $PirB^{fl/fl}$ Cre^{+} vs. $PirB^{-/-}$ Cre^{+} p=1.000
b (Figure 1J and 2H)	normality assumed (Levene's test p=0.233)	One-Way ANOVA with Bonferroni's multiple comparisons post-hoc test	0.9733	$PirB^{+/+}$ Cre^{+} vs. $PirB^{-/-}$ Cre^{+} p=0.002; $PirB^{+/+}$ Cre^{+} vs. $PirB^{fl/fl}$ Cre^{+} p=0.02; $PirB^{fl/fl}$ Cre^{+} vs. $PirB^{-/-}$ Cre^{+} p=1.000
c (Figure 1K)	normal distribution	Two-way ANOVA with repeated measures	0.2383	0.2443

d (Figure 1L)	normal distribution	Two-way ANOVA with repeated measures	0.9534	0.0574
e (Figure 2K)	normal distribution	Two-way ANOVA with repeated measures	0.0501	0.8864
f (Figure 2L)	normal distribution	Two-way ANOVA with repeated measures	0.0521	0.7799
g (Figure 3C)	normality assumed (Levene's test p=0.494)	One-Way ANOVA with Bonferroni's multiple comparisons post-hoc test	0.9988	$PirB^{+/+}$ Cre^{+} vs. $PirB^{fl/fl}$ Cre^{+} p=0.924; $PirB^{+/+}$ Cre^{+} vs. $PirB^{-/-}$ Cre^{+} p=1.000; $PirB^{fl/fl}$ Cre^{+} vs. $PirB^{-/-}$ Cre^{+} p=1.000; P23 $PirB^{+/+}$ vs. P30 $PirB^{+/+}$ p=0.004; P23 $PirB^{fl/fl}$ versus P30 $PirB^{fl/fl}$ p=0.19; P23 $PirB^{-/-}$ vs. P30 $PirB^{-/-}$ p=1.00
h (Figure 4G)	normality not assumed	Mann-Whitney	0.8509	0.0058
i(Figure 4I)	normality not assumed	Mann-Whitney	0.1634	0.3286
j (Figure 4K)	normality not assumed	Mann-Whitney	0.0961	0.4940
k (Figure 4M)	normality not assumed	Mann-Whitney	0.1855	0.3918
l (Figure 5E)	normality not assumed	Wilcoxon signed-rank test	0.9959	0.0060
m (Figure 5F)	normality not assumed	Wilcoxon signed-rank	0.1109	0.7722

		test		
n (Figure 6C)	normality assumed (Levene's test p=0.869)	One-Way ANOVA with Bonferroni's multiple comparisons post-hoc test	0.1347	$PirB^{+/+}$ Cre^{+} vs. $PirB^{fl/fl}$ Cre^{+} p=1.000; $PirB^{+/+}$ Cre^{+} vs. $PirB^{-/-}$ Cre^{+} p=1.000; $PirB^{fl/fl}$ Cre^{+} vs. $PirB^{-/-}$ Cre^{+} p=1.000

RESULTS

To examine if PirB expression specifically in pyramidal neurons is sufficient to regulate spine density, $PirB^{+/+}$, $PirB^{-/-}$, and $PirB^{fl/fl}$ mice were studied in combination with *in utero* electroporation of a GFP.Cre expression vector to target selectively a subset of excitatory pyramidal neurons in L2/3 at the time of their genesis. Because excitatory neurons from different cortical layers are generated sequentially in the cortical ventricular zone (McConnell and Kaznowski, 1991; Chen *et al*., 2008; Greig *et al*., 2013), neurons of each cortical layer can be targeted by timing *in utero* electroporations of the ventricular zone; E15.5 targets L2/3 pyramidal neurons exclusively (Saito and Nakatsuji, 2001). Glia and interneurons are not transfected since production of glial cells peaks around birth, while interneurons are generated in the ganglionic eminence and not in the ventricular zone (Anderson *et al.*, 1997; Nery, Fishell, and Corbin, 2002). Layer 2/3 pyramidal neurons are of particular interest because of the changes previously observed in $PirB^{-/-}$ mice in cellular mechanisms of synaptic plasticity at L4 to L2/3 synapses, in mEPSC frequency recorded from L2/3 neurons, and in OD plasticity as assessed in L2/3 using intrinsic signal imaging (Djurisic *et al.*, 2013).

L2/3 pyramidal neurons of germline knockout mice ($PirB^{-/-}$) have elevated dendritic spine density.

This first experiment was designed to examine if spine density on L2/3 neurons in germline knockout ($PirB^{-/-}$) mice is increased at P30. At E15.5, $PirB^{+/+}$ or $PirB^{-/-}$ embryos were injected with a DNA construct (GFP.Cre) expressing green fluorescent protein (GFP), as well as Cre recombinase under a separate promoter and subjected to electroporation. Note that this initial experiment was not performed in mice carrying a conditional allele of PirB. Consequently, neurons are labeled with GFP to permit assessment of morphology, but Cre expression does not drive excision, and instead serves as a control for subsequent experiments.

Electroporation at E15.5 results in laminar-specific GFP labeling of L2/3 pyramidal neurons in primary visual cortex at P30 (Figure 1A-D). Dendritic spines were extensively GFP+ labeled as viewed using confocal microscopy (Figure 1E-H), permitting assessment of density. Spine density on L2/3 pyramidal neurons of $PirB^{-/-}$ mice is significantly elevated, relative to $PirB^{+/+}$: spine density is 64% greater on apical dendrites in $PirB^{-/-}$ versus $PirB^{+/+}$ (Figure 1I), and 73% greater on basal dendrites. (Figure 1J). The excess dendritic spines are likely to be sites of functional synapses, since EM studies from mouse visual cortex show that over 95% of dendritic spines have machinery needed for synaptic transmission: they are positive for PSD-95 and apposed by presynaptic active zones (Arellano *et al*., 2007). Moreover, the spine density increase observed here in $PirB^{-/-}$ visual cortex is consistent with the previously reported increase in mEPSC frequency recorded from L2/3 pyramidal neurons —a sensitive measure of the density of functional excitatory synapses (Djurisic *et al.*, 2013).

These significant changes in dendritic spine density in $PirB^{-/-}$ neurons suggest that other aspects of neuronal morphology may also be altered. To examine this possibility, the dendritic

complexity of GFP+ L2/3 pyramidal neurons in visual cortex of $PirB^{+/+}$ and $PirB^{-/-}$ was assessed using Sholl analysis (Sholl, 1953). Apical and basal dendritic complexity was unaltered in $PirB^{-/-}$, relative to $PirB^{+/+}$ (Figure 1K,L). Together these observations demonstrate that the changes in mEPSC frequency observed previously (Djurisic et al, 2013) are accompanied by changes in spine density but not dendritic complexity, in L2/3 pyramidal neurons.

Sparse deletion in $PirB^{fl/fl}$ mice results in elevated spine density on isolated L2/3 pyramidal neurons.

An increase in both spine density (Figure 1) and in functional excitatory synapses (Djurisic *et al.*, 2013) is observed in L2/3 pyramidal neurons of $PirB^{-/-}$ versus $PirB^{+/+}$ mice. To examine if this increase is due to loss of PirB from the very cells where dendritic spines were counted, or due to loss of PirB in other presynaptic or non-neuronal cells, a mosaic approach was used to delete PirB from isolated L2/3 pyramidal neurons. $PirB^{fl/fl}$ mice were electroporated with GFP.Cre at E15.5, and then studied at P30 (Figure 2A-E). In $PirB^{fl/fl}$, cells expressing GFP co-express Cre recombinase, which drives excision of the floxed PirB alleles.

In a subset of $PirB^{fl/fl}$ mice electroporated with the GFP.Cre vector (see Materials and Methods), a very sparse distribution of PirB knockout neurons embedded in a "sea" of cells containing intact PirB alleles was obtained (Figure 2A-E). To quantify the sparseness of PirB deletion, the density of GFP+ cells in V1 was measured by counting the number of labeled cells in a series of concentric circles surrounding the cell selected for spine analysis (Fig. 2F). Using this "Sholl analysis", we determined that for the majority of neurons analyzed, there were almost no neighboring GFP+ neurons located within a radius of 50 microns, and then within each 50 micron increment outward from the cell under analysis, there was an average of only 1 additional

343 labeled neuron at most. In contrast, the density of labeled cells was far greater in Figure 1, where
344 a larger volume of DNA was injected. Thus, electroporation could result in a very sparse deletion
345 of PirB from isolated L2/3 pyramidal neurons, permitting us to examine a cell intrinsic function
346 for PirB in regulating dendritic spine density.

347 At P30, spine density on isolated GFP+;Cre+ L2/3 pyramidal neurons in visual cortex of
348 sparsely electroporated $PirB^{fl/fl}$ mice was significantly elevated, as compared to GFP+;Cre+
349 neurons from control $PirB^{+/+}$ mice, in which PirB excision has not occurred. In addition, density
350 was almost identical to that observed on L2/3 dendrites of GFP+;Cre+ neurons from $PirB^{-/-}$, as
351 shown in Figure 2G-J which compares data from all 3 genotypes. There are significant spine
352 density increases along both apical (52%) and basal (60%) dendrites in $PirB^{fl/fl}$ neurons that have
353 undergone recombination and lack PirB, as compared with L2/3 GFP+; Cre+ neurons in $PirB^{+/+}$
354 mice that have not undergone recombination and express PirB normally (Figure 2G, H). Multiple
355 comparison with One-way ANOVA followed by Bonferroni post-hoc test reveals significant
356 differences between density of spines on apical dendrites between $PirB^{+/+}$ vs. $PirB^{fl/fl}$ ($p=0.041$)
357 and $PirB^{+/+}$ vs. $PirB^{-/-}$ ($p=0.004$), but not $PirB^{fl/fl}$ vs. $PirB^{-/-}$ ($p=1.00$). Similar statistically
358 significant differences for basal dendritic spines were revealed by post-hoc analysis: $PirB^{+/+}$ vs.
359 $PirB^{fl/fl}$ ($p=0.02$) and $PirB^{+/+}$ vs. $PirB^{-/-}$ ($p=0.002$), but not $PirB^{fl/fl}$ vs. $PirB^{-/-}$ ($p=1.00$).

360 The dendritic arborization of GFP+;Cre+ cells in $PirB^{fl/fl}$ mice *vs.* GFP+; Cre+ cells in
361 $PirB^{+/+}$ mice was also examined. No significant differences in apical or basal dendritic Sholl
362 profiles (Sholl 1953) were observed (Figure 2K,L), underscoring a selective effect of PirB
363 deletion on spine density in isolated L2/3 neurons.
364

Dendritic spine density on L2/3 pyramidal cells in all genotypes is similar at P23 The elevated spine density observed at P30 in mice lacking PirB could arise from changes in dendritic spine formation and/or from a failure of pruning. To distinguish these possibilities, the sparse GFP.Cre electroporation experiment described above was repeated, but the density of spines was assessed one week earlier at P23, during the period of synaptic pruning and when dendritic spine density in WT visual cortex is highest based on previous Golgi and EM studies (Ruiz-Marcos and Valverde, 1969; Markus and Petit, 1987).

The dendrites and spines of L2/3 pyramidal neurons at P23 were extensively GFP-labeled (Figure 3A,B) subsequent to electroporation at E15.5. Multiple comparisons with One-way ANOVA and Bonferroni post-hoc test did not reveal any significant differences between density of spines for all 3 genotypes (Figure 3C,D). Moreover dendritic spine density for $PirB^{+/+}$ is almost twice as high at P23 (Figure 3C: ~13 spines/10 microns) than at P30 (~7 spines/10 microns). In contrast to wildtype, there are no statistically-significant differences between $PirB^{fl/fl}$ P23 vs. P30 or $PirB^{-/-}$ P23 vs. P30, strongly suggesting that spine pruning is deficient in L2/3 neurons lacking PirB.

Sparse PirB excision results in increased mEPSC frequency recorded from isolated L2/3 pyramidal neurons at P30

In $PirB^{-/-}$ germline knockout mice, the increase in spine density on L2/3 pyramidal neurons (Figure 1) is accompanied by an increase in mEPSC frequency, a measure of the density of functional excitatory synapses (Djurisic *et al.*, 2013). Is the increase in dendritic spine density observed following sparse deletion in $PirB^{fl/fl}$ similarly accompanied by an increase in mEPSC frequency? To assess the strength and number of functional excitatory synaptic inputs, the

388 frequency and amplitude of mEPSCs in acute slices from visual cortex of $PirB^{fl/fl}$ mice was
389 assessed using the patch-clamp technique (Figure 4). In this experiment, both labeled (GFP+;
390 Cre+) and unlabeled (GFP–; Cre–) neurons could be recorded and compared in the same slice
391 (Figure 4A-D); cells were also labeled via patch pipette with biocytin to confirm the pyramidal
392 identity of GFP–;Cre– cells targeted for recordings (Figure 4E,F). The frequency of mEPSCs in
393 GFP+;Cre+ neurons was 69% higher than in GFP–;Cre– controls (Figure 4G,H), with no
394 measurable change in mEPSC amplitude (Figure 4I,J).

395 Miniature EPSC frequencies and amplitudes recorded from GFP+;Cre+ neurons in
396 $PirB^{fl/fl}$ mice (Figure 4G-J) were similar to those of L2/3 pyramidal neurons in germline $PirB^{-/-}$
397 slices (Djurisic *et al.*, 2013). In addition, GFP–; Cre– neurons in $PirB^{fl/fl}$ slices had mEPSC
398 frequency and amplitudes similar to $PirB^{+/+}$ slices (*cf.* Figure 4G-J with Figure 4K-N). These
399 results indicate that the *in utero* electroporation technique by itself does not affect development
400 of functional excitatory synaptic inputs to L2/3 pyramidal neurons. To control for off-target
401 effects of Cre recombinase and GFP expression on mEPSC recordings, we also examined
402 mEPSC frequency and amplitude in $PirB^{+/+}$ tissue subsequent to electroporation with GFP.Cre.
403 In this case, Cre recombinase does not cause excision, and thus labeled and unlabeled cells differ
404 only in their expression of GFP and Cre. Results show that GFP+;Cre+ neurons in $PirB^{+/+}$ slices
405 do not differ significantly from GFP–;Cre– neurons in $PirB^{+/+}$ slices in either mEPSC frequency
406 (Figure 4K,L) or amplitude (Figure 4M,N). This experiment demonstrates that the
407 electroporation and expression of GFP and Cre in and of themselves do not alter detectably these
408 electrophysiological properties of L2/3 neurons. Together, these observations suggest that PirB is
409 required to regulate the neuron's own functional excitatory synaptic inputs, and that loss of PirB

just from the isolated cell examined is sufficient to account for changes both in density of functional synapses and spines observed in $PirB^{-/-}$ germline knockout mice.

It should be noted that the 59% increase in mEPSC frequency observed in GFP+; Cre+ neurons in $PirB^{fl/fl}$ mice (Figure 4G,H) is similar to the average 69% increase in spine density on both apical and basal dendrites (Figure 2G-J), implying that many if not all of the supernumerary dendritic spines represent sites of functional excitatory synapses.

mEPSC frequency is not altered in wild-type neighbors located within 100 µm of L2/3 pyramidal neurons lacking PirB

To test further for a cell-intrinsic effect of PirB on density of functional synaptic inputs, patch-clamp recordings were made from GFP+;Cre+ and GFP–;Cre– L2/3 pyramidal neurons that were in close proximity, separated by 100 µm or less from each other (Figure 5). Within this distance, neurons are known to have a much higher connection probability (Perin *et al.*, 2011; Hill *et al.*, 2012; Jouhanneau *et al.*, 2015). In recordings from pairs of neurons located 100 µm or less from each other (Figure 5A-D), we found that mEPSC frequencies in GFP+;Cre+ neurons were almost always greater than those for the unlabeled GFP–;Cre– neighbor (14 out of 16 pairs; Figure 5E,G). Once again, mEPSC amplitudes between GFP+;Cre+ and GFP–;Cre– neighbors did not differ significantly (Figure 5F,H). The average mEPSC frequency of GFP+;Cre+ neurons (Figure 5E) was similar to that previously recorded from L2/3 pyramidal neurons in germline $PirB^{-/-}$ mice (Djurisic *et al*., 2013). The mEPSC frequencies of neighboring GFP–;Cre– neurons (Figure 5E) were close to previously-reported levels in $PirB^{+/+}$ slices (Djurisic *et al*., 2013).

Bouton density of axons arising from L2/3 neurons lacking PirB and arborizing in L5 is unaltered

Results from experiments described above imply that PirB acting within a single L2/3 neuron can regulate the spine density of that individual neuron. To test if PirB can regulate axonal bouton density, we also analyzed at P30 the axon collaterals of L2/3 neurons that descend to cortical L5 in visual cortex (Figure 6A-B). Note that this analysis was carried out in sections from brains perfused with fixative at P30 following *in utero* electroporation at E15.5, similar to methods used in Figures 1-3. The varicosities shown at high magnification in Figure 6B are typical of en passant synaptic boutons. Bouton density of L2/3 pyramidal cell axons within L5 is not altered in GFP-labeled neurons in germline $PirB^{-/-}$ mice compared to $PirB^{+/+}$ (Figure 6C,D). Furthermore, no change in bouton density was observed in axons of isolated GFP+; Cre+ L2/3 neurons in sparsely electroporated $PirB^{fl/fl}$ mice (Figure 6C,D). Recall that these single axons arising from neurons lacking PirB arborize in a "sea" of wild type neurons and glia. Thus, this observation further supports the idea that PirB acts in a cell-intrinsic manner to regulate dendritic spine density in layer 2/3 pyramidal cells, leaving other aspects of neuronal structure intact, including axon bouton density and dendritic branching pattern.

DISCUSSION

Many factors are now known to regulate aspects of dendritic spine shape, size and stability including experience, learning and environmental enrichment (Holtmaat and Svoboda, 2009; Chen, Lu, and Zuo, 2014), but just how these external activity-dependent signals are read out into lasting changes is still relatively unclear. Here we have shown that PirB, a receptor

454 whose MHC class I ligands are regulated by neural activity (Corriveau, Huh, and Shatz, 1998;
455 Huh *et al.*, 2000), acts within individual L2/3 pyramidal neurons in a cell intrinsic manner to
456 regulate spine density and functional excitatory synapses. We have used the powerful technique
457 of *in utero* electroporation of Cre.GFP to target PirB deletion selectively to L2/3 pyramidal
458 neurons. It is remarkable that simply driving PirB excision in single isolated neurons surrounded
459 by wild type glia and wild type neurons results in a major increase in spine density within the
460 targeted neuron. This observation indicates that PirB function in individual L2/3 pyramidal
461 neurons is required to regulate spine density. It is also consistent with the previous finding that
462 spine density on L5 pyramidal cells is also elevated in mice lacking PirB (Djurisic *et al.*, 2013).
463 Together, these observations imply that PirB may regulate spine density more generally in
464 excitatory neurons of the forebrain.

465 At P30, spine density on L2/3 pyramidal neurons lacking PirB is more than 50% greater
466 than in $PirB^{+/+}$ neurons (Figures 1,2). However, just one week earlier at P23, we found that spine
467 density across all genotypes exposed to GFP.Cre at E15.5 is similar, approximately 13 spines/10
468 microns (Figure 3). Between P23 and P30, spine density on L2/3 $PirB^{+/+}$ neurons falls to about 7
469 spines/10 microns, consistent with the idea that this is a peak period for spine and synapse
470 pruning (Ruiz-Marcos and Valverde, 1969; Markus and Petit, 1987). In contrast, spine density on
471 neurons lacking PirB fails to decline and instead remains close to the P23 level. Overall, results
472 strongly suggest that PirB function is required for spine pruning during this period. Given the
473 strong evidence of a role for microglia in spine and synapse pruning (Schafer *et al.*, 2012,
474 Parkhurst *et al.*, 2013), our results also imply that without neuronal PirB expression, glia may not
475 be able to function properly to eliminate spines.

476 Several lines of evidence presented here argue that the striking increases in spine density
477 and functional synapses are not artefacts of Cre recombinase or GFP expression. First, a
478 significant increase in spine density is observed when Cre.GFP is electroporated into $PirB^{-/-}$
479 mice (Figure 1E-J). Second, a similar result is obtained when Cre.GFP is electroporated into
480 $PirB^{fl/fl}$ mice (Figure 2D-J). Third, the independent technique of mEPSC recordings revealed a
481 parallel increase in functional excitatory inputs (Figure 4,5), as signaled by the significantly
482 greater mEPSC frequency in $PirB^{-/-}$ vs $PirB^{+/+}$ neurons. Moreover, whole cell recordings of
483 mEPSCs made from isolated neurons electroporated with Cre.GFP (Figure 4,5) are
484 indistinguishable from those recorded in germline $PirB^{-/-}$ neurons (Djurisic *et al.*, 2013). Finally,
485 when Cre.GFP is electroporated into $PirB^{+/+}$ mice, mEPSCs recorded from L2/3 neurons (Figure
486 4K-N) are similar to those seen in unmanipulated $PirB^{+/+}$ mice not undergoing electroporation
487 (Djurisic *et al.*, 2013).

488 Here we have uncovered a cell-intrinsic mechanism for maintaining spine density and
489 excitatory synaptic input below an upper bound. L2/3 neurons lacking PirB have as much as a
490 73% greater spine density than $PirB^{+/+}$ neurons (Figure 1,2). The corresponding increase in
491 mEPSC frequency (Figure 4) suggests that many of the spines on isolated $PirB^{-/-}$ cells are
492 functional, a finding similar to what has been observed on the L5 pyramidal neurons in $PirB^{-/-}$
493 mice (Djurisic *et al.*, 2013). Moreover, we observed that neurons with intact PirB alleles have
494 lower mEPSC frequencies than their isolated neighbors lacking PirB (Figure 5). This observation
495 is one of the strongest arguments for a cell autonomous role for PirB in L2/3 pyramidal neurons.
496 The fact that mEPSC frequency in wild type neighbors is indistinguishable from that recorded in
497 L2/3 $PirB^{+/+}$ mice, and that mEPSC frequency in isolated $PirB^{-/-}$ cells is indistinguishable from

498 that recorded in L2/3 neurons in PirB$^{-/-}$ germline knockout mice, is additional support for this
499 conclusion.

500 The term "cell autonomous" is used here explicitly in reference to a role for PirB in
501 regulating spine density on L2/3 pyramidal neurons. There are several other examples in which
502 spine density is thought to be regulated by cell-autonomous mechanisms, including NgR1 in the
503 cortex (Akbik *et al.*, 2013) and Sema5A in the hippocampus (Duan *et al.*, 2014). In all of these
504 cases, including PirB, the conclusion regarding cell-autonomous function could not have been
505 achieved without mosaic analysis *in vivo* or *in vitro*. PirB may also have non-cell autonomous
506 functions. For example, the increase in mEPSC frequency recorded in isolated neurons lacking
507 PirB implies that there has been a parallel increase in the number of presynaptic boutons, which
508 likely derive from a vast majority of PirB$^{+/+}$ neurons. Thus, the spine density increase appears to
509 drive a transynaptic increase in functional inputs: a non-cell autonomous effect. This
510 interpretation is also consistent with the finding here that in the sparse electroporation
511 experiments, the axon bouton density of neurons lacking PirB does not differ from PirB$^{+/+}$
512 (Figure 6). These mutant axons are embedded in a sea of PirB$^{+/+}$ neurons possessing normal
513 spine density. A non-cell autonomous role for PirB in regulating presynaptic boutons would
514 predict that the density of axonal inputs belonging to PirB$^{-/-}$ neurons should be wild type- exactly
515 what we have observed.

516 There is a growing list of molecules known to regulate spines and excitatory synaptic
517 inputs to cerebral cortical pyramidal cells. For instance, FMRP regulates spine density and
518 maturation; in the knockout, spine density is increased but spines remain thin and immature, and
519 can be rescued by reducing mGluR5 expression (Dölen *et al.*, 2007). Another receptor, DR6,
520 regulates the density of axonal boutons and sprouting following activity-dependent deprivation

but there is no known effect on the normal developmental spine pruning process (Marik *et al.*, 2013). NgR1 is thought to regulate the density of mature dendritic spines (Karlsson *et al.*, 2016); however there is currently some disagreement about its exact role in dendritic spine and axonal bouton turnover (Akbik *et al.*, 2013, Park *et al.*, 2014, Frantz *et al.*, 2016). Many downstream effectors have been identified and studied, including Rho GTPases (Murakoshi, Wang, and Yasuda, 2011, Colgan and Yasuda, 2014) and the actin cytoskeleton (Kim *et al.*, 2013, Kellner *et al.*, 2016). In contrast, our studies suggest that PirB acts to keep spine density below a ceiling level (Djurisic et al, 2013), with no apparent effect either on the distribution of spine types (Bochner *et al.*, 2014) or on overall dendritic morphology (Figure 1K,L; 2K,L). Spine motility on L5 pyramidal neurons lacking PirB is also decreased (Djurisic *et al.*, 2013), implying a connection between PirB and downstream signaling to cofilin and the actin cytoskeleton (Kim *et al.*, 2013). Clearly, every aspect of the spine is tightly regulated to enable experience-dependent changes to be encoded structurally. Together, the results of our studies suggest that PirB is needed to match spine density and excitatory synaptic function to activity levels within cortical circuits, thereby providing headroom for the cell to encode additional experiences at new synapses.

REFERENCES

Adelson JD, Barreto GE, Xu L, Kim T, Brott BK, Ouyang YB, Naserke T, Djurisic M, Xiong X, Shatz CJ, Giffard RG (2012). Neuroprotection from stroke in the absence of MHCI or PirB. Neuron 73:1100-7.

543 Adelson JD, Sapp RW, Brott BK, Lee H, Miyamichi K, Luo L, Cheng S, Djurisic M, Shatz CJ
544 (2016). Developmental Sculpting of Intracortical Circuits by MHC Class I H2-Db and H2-Kb.
545 Cereb Cortex 26:1453-63.
546
547 Akbik FV, Bhagat SM, Patel PR, Cafferty WB, Strittmatter SM (2013). Anatomical plasticity of
548 adult brain is titrated by Nogo Receptor 1. Neuron 77:859–866.
549
550 Anderson SA, Eisenstat DD, Shi L, Rubenstein JL (1997). Interneuron migration from basal
551 forebrain to neocortex: dependence on Dlx genes. Science 278:474-6.
552
553 Andreu-Agullo C, Maurin T, Thompson CB, Lai EC (2011). Ars2 maintains neural stem-cell
554 identity through direct transcriptional activation of Sox2. Nature 481:195-8.
555
556 Arellano JI, Benavides-Piccione R, Defelipe J, Yuste R (2007). Ultrastructure of dendritic
557 spines: correlation between synaptic and spine morphologies. Front Neurosci 1:131-43.
558
559 Bochner DN, Sapp RW, Adelson JD, Zhang S, Lee H, Djurisic M, Syken J, Dan Y, Shatz CJ
560 (2014). Blocking PirB up-regulates spines and functional synapses to unlock visual cortical
561 plasticity and facilitate recovery from amblyopia. Sci Transl Med. 6:258ra140.
562
563 Bukhari N, Burman PN, Hussein A, Demars MP, Sadahiro M, Brady DM, Tsirka SE, Russo SJ,
564 Morishita H (2015). Unmasking Proteolytic Activity for Adult Visual Cortex Plasticity by the
565 Removal of Lynx1. J Neurosci 35:12693-702.

566

567 Chen B, Wang SS, Hattox AM, Rayburn H, Nelson SB, McConnell SK (2008). The Fezf2-Ctip2
568 genetic pathway regulates the fate choice of subcortical projection neurons in the developing
569 cerebral cortex. PNAS 105:11382-7.

570

571 Chen CC, Lu J, Zuo Y (2014). Spatiotemporal dynamics of dendritic spines in the living brain.
572 Front Neuroanat 8:28.

573

574 Colgan LA, Yasuda R (2014). Plasticity of dendritic spines: subcompartmentalization of
575 signaling. Annu Rev Physiol 76:365-85.

576

577 Corriveau RA, Huh GS, Shatz CJ (1998). Regulation of class I MHC gene expression in the
578 developing and mature CNS by neural activity. Neuron 21:505-20.

579

580 Crozier RA, Wang Y, Liu CH, Bear MF (2007). Deprivation-induced synaptic depression by
581 distinct mechanisms in different layers of mouse visual cortex. PNAS 104:1383-8.

582

583 De Paola V, Holtmaat AJGD, Knott G, Song S, Wilbrecht L, Caroni P, Svoboda K (2006). Cell
584 type-specific structural plasticity of axonal branches and boutons in the adult neocortex. Neuron
585 49:861-875.

586

587 Djurisic M, Vidal GS, Mann M, Aharon A, Kim T, Ferrao Santos A, Zuo Y, Hübener M, Shatz
588 CJ (2013). PirB regulates a structural substrate for cortical plasticity. PNAS 110:20771-6.

589

590 Dölen G, Osterweil E, Rao BS, Smith GB, Auerbach BD, Chattarji S, Bear MF (2007).
591 Correction of fragile X syndrome in mice. Neuron 56:955-62.

592

593 Duan Y, Wang SH, Song J, Mironova Y, Ming GL, Kolodkin AL, Giger RJ (2014). Semaphorin
594 5A inhibits synaptogenesis in early postnatal- and adult-born hippocampal dentate granule cells.
595 eLife 3:e04390.

596

597 Faul F, Erdfelder E, Lang A-G, Buchner A (2007). G*Power 3: A flexible statistical power
598 analysis program for the social, behavioral, and biomedical sciences. Behavior Research
599 Methods 39:175-191.

600

601 Faul F, Erdfelder E, Buchner A, Lang A-G (2009). Statistical power analyses using G*Power
602 3.1: Tests for correlation and regression analyses. Behavior Research Methods 41:1149-1160.

603

604 Frantz MG, Kast RJ, Dorton HM, Chapman KS, McGee AW (2016). Nogo receptor 1 limits
605 ocular dominance plasticity but not turnover of axonal boutons in a model of amblyopia. Cereb
606 Cortex 26:1975-85.

607

608 Fu M, Yu X, Lu J, Zuo Y (2012). Repetitive motor learning induces coordinated formation of
609 clustered dendritic spines in vivo. Nature 483:92–95.

610

611 Gordon JA, Stryker MP (1996). Experience-dependent plasticity of binocular responses in the
612 primary visual cortex of the mouse. J Neurosci 16:3274-86.
613
614 Greig LC, Woodworth MB, Galazo MJ, Padmanabhan H, Macklis JD (2013). Molecular logic of
615 neocortical projection neuron specification, development and diversity. Nat Rev Neurosci
616 14:755-69.
617
618 Hayashi-Takagi A, Yagishita S, Nakamura M, Shirai F, Wu YI, Loshbaugh AL, Kuhlman B,
619 Hahn KM, Kasai H (2015). Labelling and optical erasure of synaptic memory traces in the motor
620 cortex. Nature 525:333-8.
621
622 Hill SL, Wang Y, Riachi I, Schürmann F, Markram H (2012). Statistical connectivity provides a
623 sufficient foundation for specific functional connectivity in neocortical neural microcircuits.
624 PNAS 109:E2885-94.
625
626 Hippenmeyer S, Youn YH, Moon HM, Miyamichi K, Zong H, Wynshaw-Boris A, Luo L (2010).
627 Genetic mosaic dissection of Lis1 and Ndel1 in neuronal migration. Neuron 68:695-709.
628
629 Hofer SB, Mrsic-Flogel TD, Bonhoeffer T, Hübener M (2006). Prior experience enhances
630 plasticity in adult visual cortex. Nat Neurosci 9:127-132.
631
632 Hofer SB, Mrsic-Flogel TD, Bonhoeffer T, Hübener M (2009). Experience leaves a lasting
633 structural trace in cortical circuits. Nature 457:313-318.

Holtmaat A, Svoboda K (2009). Experience-dependent structural synaptic plasticity in the mammalian brain. Nat Rev Neurosci 10:647-58.

Huh GS, Boulanger LM, Du H, Riquelme PA, Brotz TM, Shatz CJ (2000). Functional requirement for class I MHC in CNS development and plasticity. Science 290:2155-9.

Jouhanneau JS, Kremkow J, Dorrn AL, Poulet JF (2015). In Vivo Monosynaptic Excitatory Transmission between Layer 2 Cortical Pyramidal Neurons. Cell Rep 13:2098-106.

Karlsson TE, Smedfors G, Brodin AT, Åberg E, Mattsson A, Högbeck I, Wellfelt K, Josephson A, Brené S, Olson L (2016). NgR1: A Tunable Sensor Regulating Memory Formation, Synaptic, and Dendritic Plasticity. Cereb Cortex 26:1804-17.

Kellner Y, Fricke S, Kramer S, Iobbi C, Wierenga CJ, Schwab ME, Korte M, Zagrebelsky M (2016). Nogo-A controls structural plasticity at dendritic spines by rapidly modulating actin dynamics. Hippocampus (epub ahead of print).

Kim T, Vidal GS, Djurisic M, William CM, Birnbaum ME, Garcia KC, Hyman BT, Shatz CJ (2013). Human LilrB2 is a β-amyloid receptor and its murine homolog PirB regulates synaptic plasticity in an Alzheimer's model. Science 341:1399–1404.

656 Lu W, Bushong EA, Shih TP, Ellisman MH, Nicoll RA (2013). The cell-autonomous role of
657 excitatory synaptic transmission in the regulation of neuronal structure and function. Neuron
658 78:433-9.
659
660 Ma L, Qiao Q, Tsai JW, Yang G, Li W, Gan WB (2016). Experience-dependent plasticity of
661 dendritic spines of layer 2/3 pyramidal neurons in the mouse cortex. Dev Neurobiol 76:277-86.
662
663 Marik SA, Olsen O, Tessier-Lavigne M, Gilbert CD (2013). Death receptor 6 regulates adult
664 experience-dependent cortical plasticity. J Neurosci 33:14998–15003.
665
666 Markus EJ, Petit TL (1987). Neocortical synaptogenesis, aging, and behavior: lifespan
667 development in the motor-sensory system of the rat. Exp Neurol 96:262-78.
668
669 McConnell SK, Kaznowski CE (1991). Cell cycle dependence of laminar determination in
670 developing neocortex. Science 254:282–285.
671
672 McGee AW, Yang Y, Fischer QS, Daw NW, Strittmatter SM (2005). Experience-Driven
673 Plasticity of Visual Cortex Limited by Myelin and Nogo Receptor. Science 309:2222.
674
675 Morishita H, Miwa JM, Heintz N, Hensch TK (2010). Lynx1, a cholinergic brake, limits
676 plasticity in adult visual cortex. Science 330:1238.
677

678 Muhia M, Willadt S, Yee BK, Feldon J, Paterna JC, Schwendener S, Vogt K, Kennedy MB,
679 Knuesel I (2012). Molecular and behavioral changes associated with adult hippocampus-specific
680 SynGAP1 knockout. Learn Mem 19:268-81.
681
682 Murakoshi H, Wang H, Yasuda R (2011). Local, persistent activation of Rho GTPases during
683 plasticity of single dendritic spines. Nature 472:100-4.
684
685 Nery S, Fishell G, Corbin JG (2002). The caudal ganglionic eminence is a source of distinct
686 cortical and subcortical cell populations. Nat Neurosci 5:1279-87.
687
688 Park JI, Frantz MG, Kast RJ, Chapman KS, Dorton HM, Stephany CÉ, Arnett MT, Herman DH,
689 McGee AW (2014). Nogo receptor 1 limits tactile task performance independent of basal
690 anatomical plasticity. PLoS One 9:e112678.
691
692 Parkhurst CN, Yang G, Ninan I, Savas JN, Yates JR 3rd, Lafaille JJ, Hempstead BL, Littman
693 DR, Gan WB (2013). Microglia promote learning-dependent synapse formation through brain-
694 derived neurotrophic factor. Cell 155:1596-609.
695
696 Paxinos G, Franklin KBJ (2008). The mouse brain in stereotaxic coordinates, 3rd edition.
697 Academic Press.
698
699 Perin R, Berger TK, Markram H (2011). A synaptic organizing principle for cortical neuronal
700 groups. PNAS 108:5419-24.

Pizzorusso T, Medini P, Berardi N, Chierzi S, Fawcett JW, Maffei L (2002). Reactivation of ocular dominance plasticity in the adult visual cortex. Science 298:1248-51.

Qin JY, Zhang L, Clift KL, Hulur I, Xiang AP, Ren B-Z, Lahn BT (2010). Systematic comparison of constitutive promoters and the doxycycline-inducible promoter. PLoS ONE 5 (5): e10611 doi: 10.1371/journal.pone.0010611.

Ruiz-Marcos A, Valverde F (1969). The temporal evolution of the distribution of dendritic spines in the visual cortex of normal and dark raised mice. Exp Brain Res 8:284-94.

Saito T, Nakatsuji N (2001). Efficient gene transfer into the embryonic mouse brain using in vivo electroporation. Dev Biol 240:237-46.

Saito T (2006). In vivo electroporation in the embryonic mouse central nervous system. Nat Protoc 1:1552-8.

Schafer DP, Lehrman EK, Kautzman AG, Koyama R, Mardinly AR, Yamasaki R, Ransohoff RM, Greenberg ME, Barres BA, Stevens B (2012). Microglia sculpt postnatal neural circuits in an activity and complement-dependent manner. Neuron 74:691–705.

722 Scotto-Lomassese S, Nissant A, Mota T, Néant-Féry M, Oostra BA, Greer CA, Lledo PM,
723 Trembleau A, Caillé I (2011). Fragile X mental retardation protein regulates new neuron
724 differentiation in the adult olfactory bulb. J Neurosci 31:2205-15.
725
726 Sholl DA (1953). Dendritic organization in the neurons of the visual and motor cortices of the
727 cat. J Anat 87:387-406.
728
729 Syken J, Grandpre T, Kanold PO, Shatz CJ (2006). PirB restricts ocular-dominance plasticity in
730 visual cortex. Science 313:1795-800.
731
732 Tabata H, Nakajima K (2001). Efficient in utero gene transfer system to the developing mouse
733 brain using electroporation: visualization of neuronal migration in the developing cortex.
734 Neuroscience 103:865-72.
735
736 Xu J, Pang ZP, Shin OH, Südhof TC (2009a). Synaptotagmin-1 functions as a Ca2+ sensor for
737 spontaneous release. Nat Neurosci 12:759-66.
738
739 Xu T, Yu X, Perlik AJ, Tobin WF, Zweig JA, Tennant K, Jones T, Zuo Y (2009b). Rapid
740 formation and selective stabilization of synapses for enduring motor memories. Nature 462:915–
741 919.
742

743 **FIGURE LEGENDS**

Figure 1. Density of dendritic spines on L2/3 pyramidal neurons is greater in visual cortex of germline PirB$^{-/-}$ mice than in PirB$^{+/+}$ at postnatal day 30 (P30). A. A low-magnification fluorescence micrograph of P30 mouse visual cortex showing GFP expression (green) in cells in L2/3 after GFP.Cre electroporation at E15.5. B, C. Higher magnification views of boxed region shown in A; DAPI nuclear counterstain (B) shows that most of the GFP+ neurons (C) are in layer 2 and upper layer 3. Soluble GFP fills the cells: cell bodies and dendrites, as well as descending axons clustering within layer 5 are all clearly visible. D. High magnification maximum intensity projection of boxed region shown in C. Dendritic spines and axonal boutons are visible. E, F, G, H. High magnification fluorescent micrographs showing apical (E, G) and basal (F, H) dendritic spines in PirB$^{+/+}$ and PirB$^{-/-}$ mice. I. Apical dendritic spine density on L2/3 pyramidal neurons of PirB$^{-/-}$ visual cortex is elevated compared to PirB$^{+/+}$ (PirB$^{+/+}$ GFP+;Cre+: 7.0 ± 0.6 dendritic spines/10 µm of dendrite length, n=9 cells, 5 mice; PirB$^{-/-}$: GFP+;Cre+: 11.5 ± 1.0, n = 13 cells, 5 mice, p=0.004[a], One-way ANOVA with post-hoc Bonferroni's multiple comparisons). J. Basal dendritic spine density is also increased in PirB$^{-/-}$ compared to PirB$^{+/+}$ (PirB$^{+/+}$ GFP+;Cre+: 6.6 ± 0.6 dendritic spines/10 µm of dendrite length, n=9 cells, 5 mice; PirB$^{-/-}$ GFP+;Cre+: 11.4 ± 1.1, n=10 cells, 5 mice, p=0.002[b], One-way ANOVA with post-hoc Bonferroni's multiple comparisons). K, L. Sholl analysis reveals no significant changes in apical (K) or basal (L) dendritic branching between PirB$^{+/+}$ and PirB$^{-/-}$ L2/3 neurons (PirB$^{+/+}$ GFP+;Cre+: n=5 cells, 3 mice; PirB$^{-/-}$ GFP+;Cre+: n=8 cells, 5 mice; K: p=0.2443[c], L: p=0.0574[d], Two-way ANOVA with repeated measures). ** p<0.01;; Calibration bars: 0.2 mm (A), 50 µm (B,C), 25 µm (D), 3 µm (E, F, G, H).

Figure 2. Dendritic spine density at P30 is elevated on isolated PirB$^{-/-}$ neurons in layer 2/3 after sparse excision of PirB at E15.5. A, B. Fluorescent micrographs at postnatal day 30 (P30) of nuclear counterstain (DAPI) (A) and an isolated L2/3 pyramidal neuron electroporated with GFP.Cre (B) from a visual cortex section from a P30 PirB$^{fl/fl}$ mouse. C. High-magnification maximum intensity projection of the boxed area in (B). D, E. Zoomed-in high magnification micrographs of portions of apical (D) and basal (E) dendrites showing dendritic spines in PirB$^{fl/fl}$ mice. F. Number of neighboring GFP+;Cre+ cells as a function of distance from a neuron of interest in PirB$^{fl/fl}$ tissue (n=8 cells, 7 mice). The graph shows that, on average, there was only one GFP+;Cre+ cell in every 50 micron increment analyzed. G. Spine density on apical dendrites is greater in GFP+;Cre+ neurons from PirB$^{fl/fl}$ mice than PirB$^{+/+}$ mice. (PirB$^{+/+}$: 7.0 ± 0.6 dendritic spines/10 µm of dendritic length, n=9 cells, 5 mice, same data as in Figure 1I; PirB$^{fl/fl}$, GFP+;Cre+: 10.6 ± 0.8, n=9 cells, 7 mice; PirB$^{-/-}$, GFP+;Cre+: 11.5 ± 1.0, n = 13 cells, 5 mice, same data as in Figure 1I; PirB$^{+/+}$ vs. PirB$^{fl/fl}$ p=0.041[a], PirB$^{fl/fl}$ vs. PirB$^{-/-}$ p=1.000[a], One-way ANOVA with post-hoc Bonferroni's multiple comparisons.) H. Basal dendritic spine density is greater in GFP+; Cre+ neurons from PirB$^{fl/fl}$ mice than PirB$^{+/+}$ mice. (PirB$^{+/+}$: 6.6 ± 0.6 dendritic spines/10 µm of dendritic length, n=9 cells, 5 mice, data from Figure 1J; PirB$^{fl/fl}$, GFP+;Cre+: 10.6 ± 1.0, n=8 cells, 7 mice; PirB$^{-/-}$, GFP+;Cre+: 11.4 ± 1.1, n=10 cells, 5 mice, data from Figure 1J; PirB$^{+/+}$ vs. PirB$^{fl/fl}$ p=0.02[b], PirB$^{fl/fl}$ vs. PirB$^{-/-}$ p=1.000[b], One-way ANOVA with post-hoc Bonferroni's multiple comparisons.) I. Cumulative histogram (by cell) of data presented in (G). J. Cumulative histogram (by cell) of data presented in (H). K, L. Sholl analysis reveals no significant changes in apical (K) or basal (L) dendritic branching between GFP+;Cre+ L2/3 neurons from PirB$^{+/+}$ and PirB$^{fl/fl}$ mice (K: PirB$^{+/+}$ n=5 cells, 3 mice, data from Figure 1K; PirB$^{fl/fl}$ n=5 cells, 3 mice, p=0.8864[c]; L: PirB$^{+/+}$ n=5 cells, 3 mice, data from Figure 1L, PirB$^{fl/fl}$

n=4 cells, 3 mice, p=0.7799[f]; Two-way ANOVA with repeated measures). *p<0.05; ** p<0.01 Calibration bars: 100 μm (A, B); 25 μm (C); 3 μm (D, E).

Figure 3. At P23, dendritic spine density on L2/3 pyramidal cells in PirB$^{-/-}$ visual cortex is similar to that of PirB$^{+/+}$. A. Fluorescent micrograph at P23, an age near the onset of spine pruning, showing an isolated L2/3 pyramidal neuron electroporated with GFP.Cre at E15.5. B. High-magnification maximum intensity projection of boxed area in (A) showing spines on basal dendrites of GFP+;Cre+ L2/3 neuron. C. Basal dendrite spine density is higher in PirB$^{+/+}$ at P23 than in PirB$^{+/+}$ at P30 (P30 data indicated by dotted line; data from Figure 2H); spine density from P23 PirB$^{+/+}$ is not different from PirB$^{fl/fl}$ or PirB$^{-/-}$.(P23 PirB$^{+/+}$: 12.66 ± 1.5, n=6 cells, 3 mice; P23 PirB$^{fl/fl}$: 14.43 ± 0.9, n=7 cells, 5 mice; P23 PirB$^{-/-}$: 13.39 ± 1.1, n=8 cells, 4 mice. P23 PirB$^{+/+}$vs. P23 PirB$^{-/-}$ p=1.000[g], P23 PirB$^{+/+}$ vs. P23 PirB$^{fl/fl}$ p=0.924[g], P23 PirB$^{fl/fl}$ vs. PirB$^{-/-}$ p=1.000[g], One-way ANOVA with post-hoc Bonferroni's multiple comparisons. P23 PirB$^{+/+}$ vs. P30 PirB$^{+/+}$ p=0.004[g], P23 PirB$^{fl/fl}$ vs. P30 PirB$^{fl/fl}$ p=0.19[g], P23 PirB$^{-/-}$ vs. P30 PirB$^{-/-}$ p=1.00[g], One-way ANOVA with post-hoc Bonferroni's multiple comparisons.) D. Cumulative histogram (by cell) of data presented in (C). Calibration bars: 50 μm (A) 5 μm (B).

Figure 4. Sparse excision of PirB from PirB$^{fl/fl}$ at E15.5 increases mEPSC frequency but not amplitude in L2/3 pyramidal neurons in P30 visual cortex. A, C. Combined differential interference contrast and fluorescence micrographs of neurons in visual cortex used for whole cell recordings of mEPSCs, showing GFP–;Cre– cells (A) and an isolated GFP+;Cre+ cell (C). B, D. Example mEPSC traces from GFP–;Cre– (B) or GFP+;Cre+ (D) L2/3 pyramidal neurons from primary visual cortex slices of P30 PirB$^{fl/fl}$ mice. E. Fluorescent micrograph showing a L2/3

pyramidal neuron filled with biocytin during mEPSC recording, and visualized with Texas Red - conjugated avidin. F. Zoomed-in maximum intensity projection of the boxed area in (E), showing apical dendritic spines. G. In $PirB^{fl/fl}$ mice, mEPSC frequency is increased in GFP+;Cre+ cells compared to GFP-;Cre– cells. (GFP-;Cre– : 16.91 ± 2.28 Hz, n=17 cells, 14 slices, 8 mice; GFP+;Cre+: 28.51 ± 2.89 Hz, n=22 cells, 14 slices, 8 mice, p=0.0058[h], Mann-Whitney.) H. Cumulative histogram (by cell) of data presented in (G). I. mEPSC amplitude does not differ between GFP-;Cre– and GFP+;Cre+ cells in $PirB^{fl/fl}$ mice. (GFP-; Cre–: 13.18 ± 0.97 pA, n=17, cells, 14 slices, 8 mice, GFP+;Cre+: 14.32 ± 0.64 pA, n=22 cells, 14 slices, 8 mice, p=0.3286[i], Mann-Whitney.) J. Cumulative histogram (by cell) of data presented in (I). K. In control $PirB^{+/+}$ mice, electroporation of GFP.Cre did not result in an increase in mEPSC frequency in GFP+;Cre+ relative to GFP-;Cre–, as expected (GFP-;Cre–: 12.53 ± 2.55 Hz, n=11 cells, 11 slices, 6 mice; GFP+;Cre+: 15.01 ± 2.76, n=13 cells, 11 slices, 6 mice; p=0.4940[j], Mann-Whitney.) L. Cumulative histogram of data presented in (K). M. In control $PirB^{+/+}$ mice, mEPSC amplitudes are not different between GFP+;Cre+ and GFP-;Cre– cells (GFP-;Cre–: 11.28 ± 1.26 pA, n=11 cells, 11 slices, 6 mice; GFP+;Cre+: 9.73 ± 0.69, n=13 cells, 11 slices, 6 mice; p=0.3918[k], Mann-Whitney.) N. Cumulative histogram of data (by cell) presented in (M). Calibration bars: 25 μm (A,C); 20 μm (E); 5 μm (F). ** $p<0.01$

Figure 5. Sparse excision of PirB at E15.5 increases mEPSC frequency of targeted L2/3 pyramidal neurons in visual cortex, but not in unmanipulated neighboring cells. A, B. Combined differential interference contrast and fluorescence micrograph of visual cortical slice used for whole cell recordings, showing electrode targeting a GFP-;Cre- cell (A) or an isolated GFP+;Cre+ cell (B). C, D. Example traces of mEPSC events in GFP–;Cre– (C) or GFP+;Cre+

(D) L2/3 pyramidal neurons in slices of visual cortex from P30 $PirB^{fl/fl}$ mice. E. In $PirB^{fl/fl}$ mice, GFP+;Cre+ cells have higher mEPSC frequency compared to GFP–;Cre– cells. (GFP-;Cre–: 16.36 ± 2.38 Hz, n=16 cells, 10 slices, 7 mice; GFP+;Cre+: 28.26 ± 4.60, n=16 cells, 10 slices, 7 mice; p=0.0060[l], Wilcoxon signed-rank test.) F. mEPSC amplitude is not significantly different in GFP–-; Cre– vs. GFP+; Cre+ cells. (GFP-;Cre–: 13.49 ± 1.01 pA, n=16 cells, 10 slices, 7 mice; GFP+;Cre+ 14.10 ± 0.77, n=16 cells, 10 slices, 7 mice; p=0.7722[m], Wilcoxon signed-rank test) G, H. Cumulative histograms (by cell) of data presented in (E) and (F), respectively. Calibration bar: 25 μm (A, B) ** p<0.01

Figure 6. Bouton density on intracortical axons of L2/3 pyramidal cells is not changed with either sparse or germline deletion of PirB. A. Example fluorescence micrograph of boutons along axons within layer 5 arising from L2/3 pyramidal neurons. B. High-magnification maximum intensity projection of boxed area in (A). C. Bouton density is not different between $PirB^{+/+}$, $PirB^{fl/fl}$, and $PirB^{-/-}$ L2/3 pyramidal neurons electroporated with GFP.Cre ($PirB^{+/+}$: 3.3 ± 0.2, n=8 cells, 3 mice; $PirB^{fl/fl}$ 3.6 ± 0.3, n=9 cells, 5 mice; $PirB^{-/-}$ 3.3 ± 0.2, n=13 cells, 5 mice. $PirB^{+/+}$ vs. $PirB^{-/-}$ p=1.000[n], $PirB^{+/+}$ vs. $PirB^{fl/fl}$ p=1.000[n], $PirB^{fl/fl}$ vs. $PirB^{-/-}$ p=1.000[n], One-way ANOVA with post-hoc Bonferroni's multiple comparisons). D. Cumulative histogram of data (by cell) presented in Calibration bars: 50 μm (A); 5 μm (B).

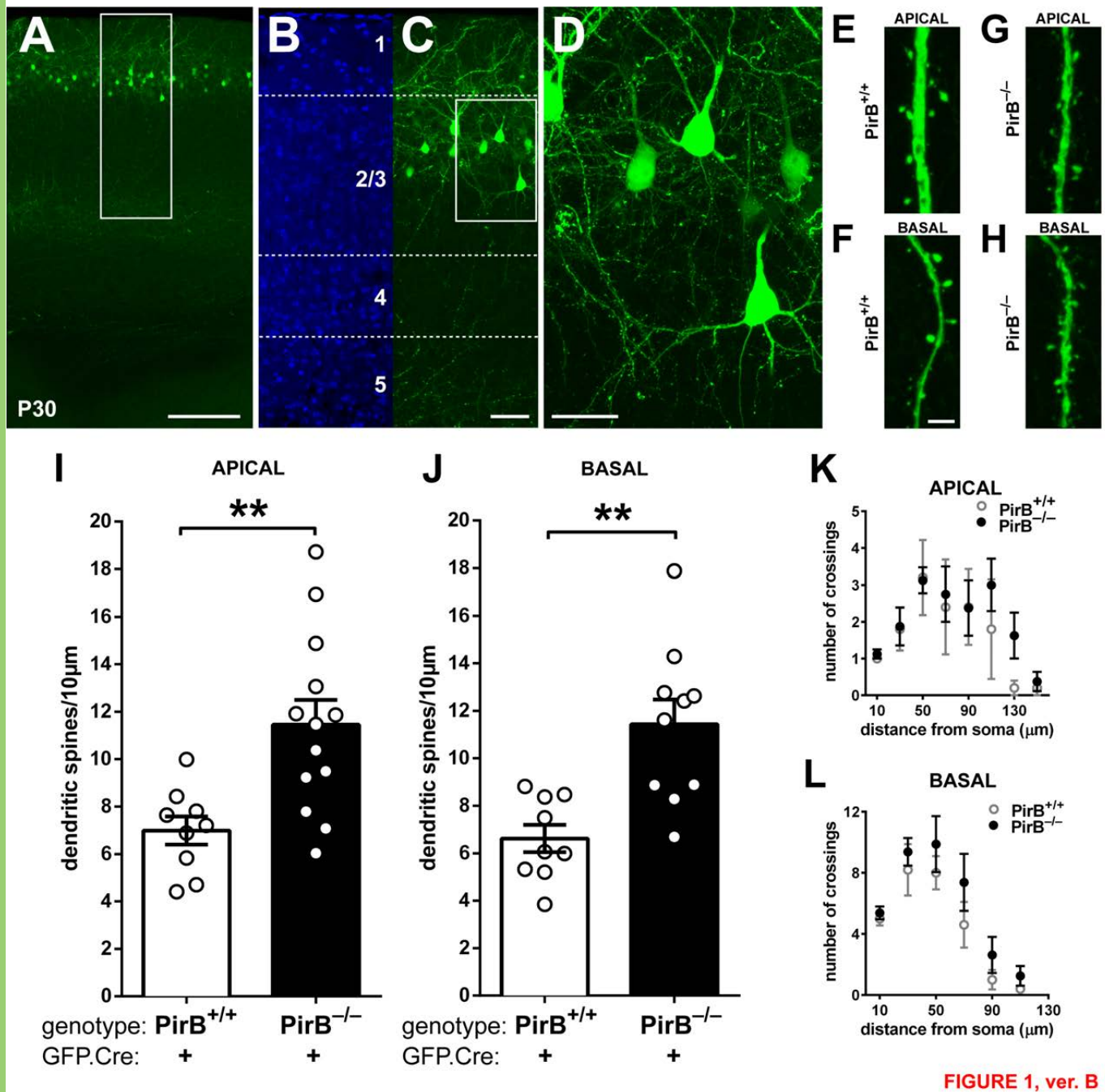

FIGURE 1, ver. B

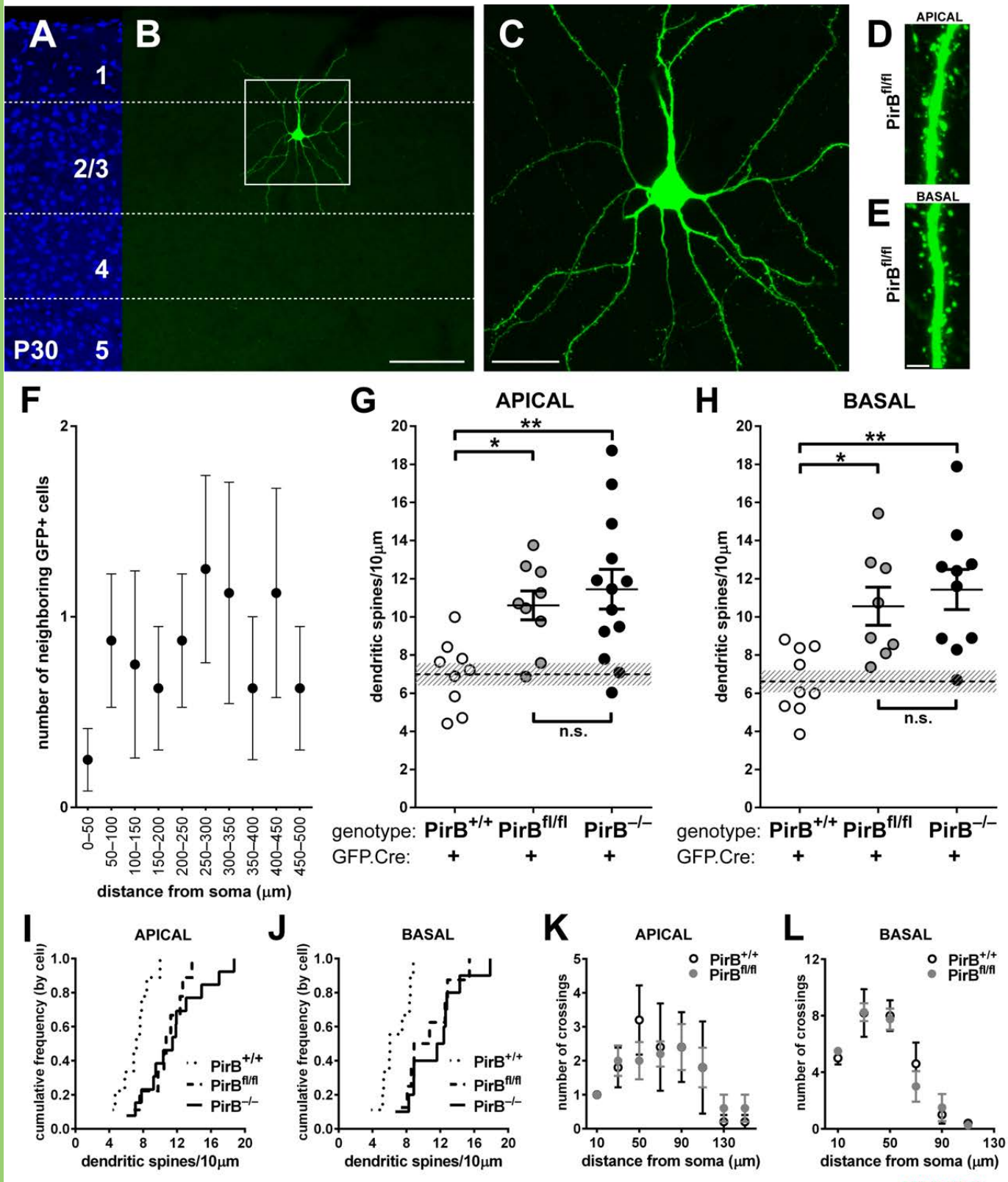

FIGURE 2

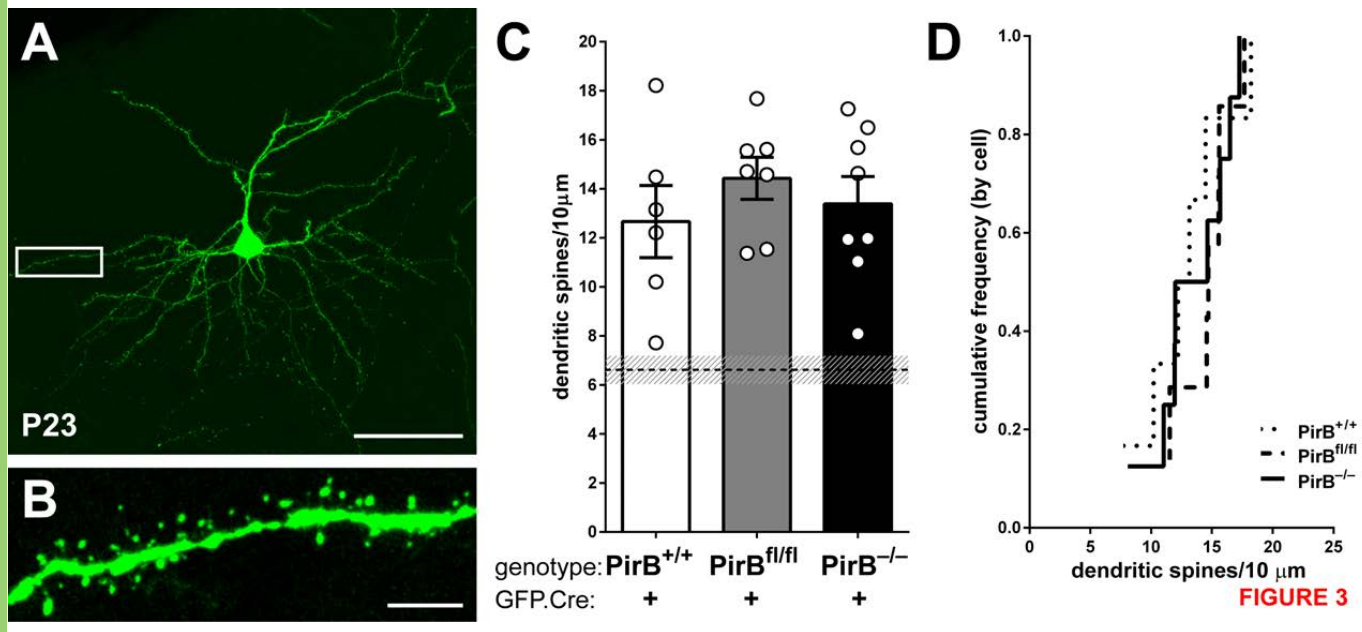

FIGURE 3

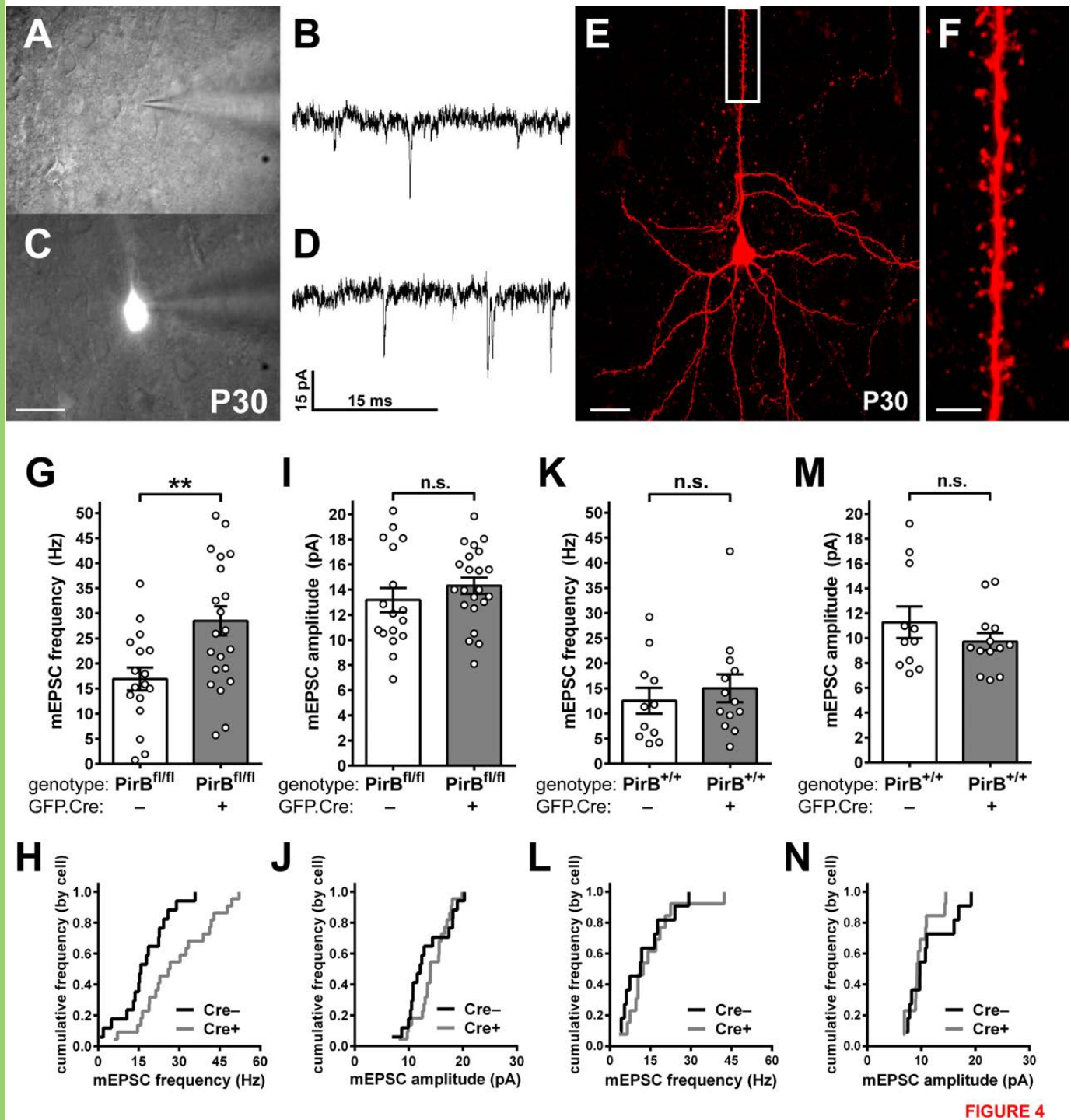

FIGURE 4

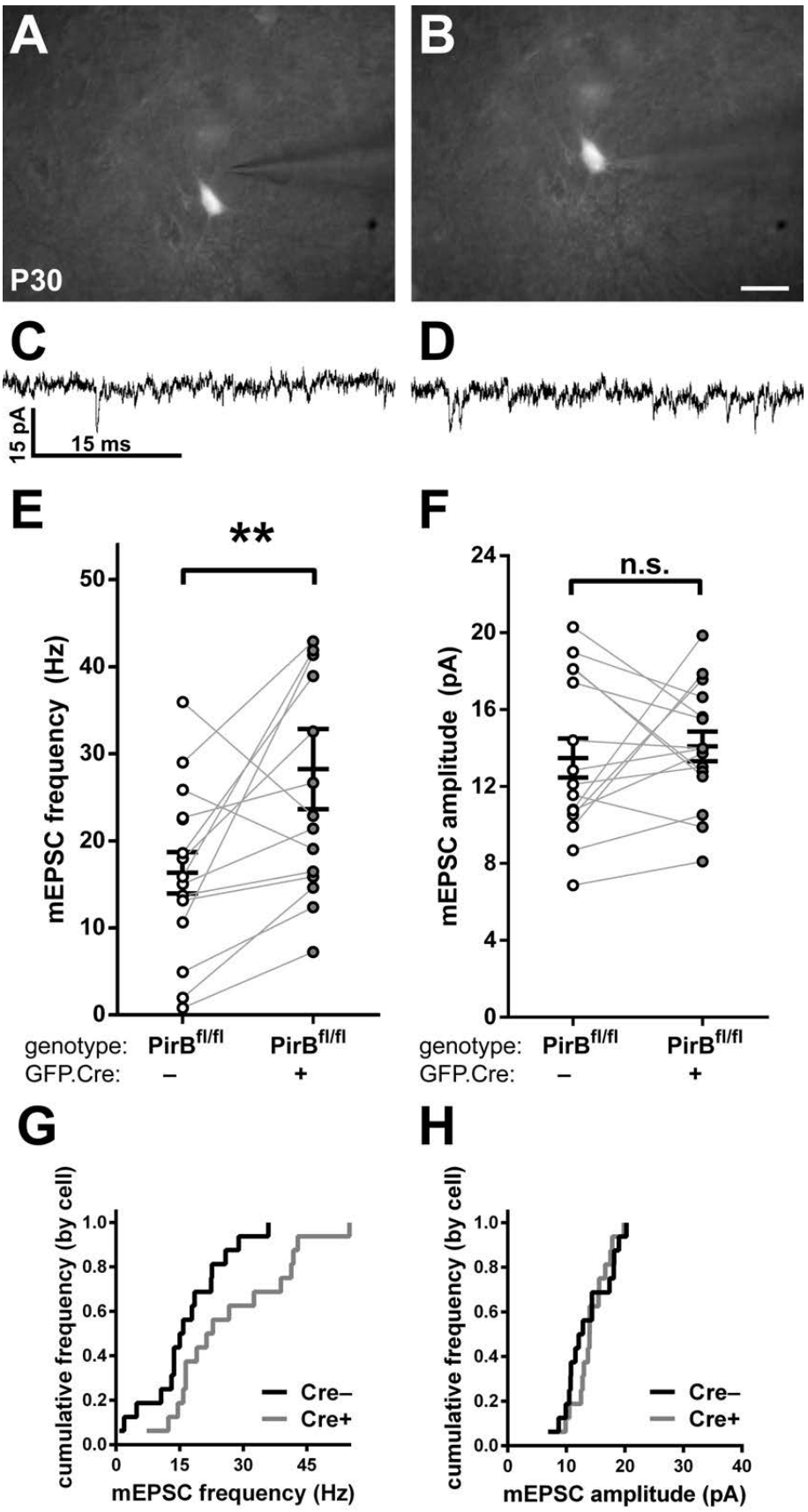

FIGURE 5

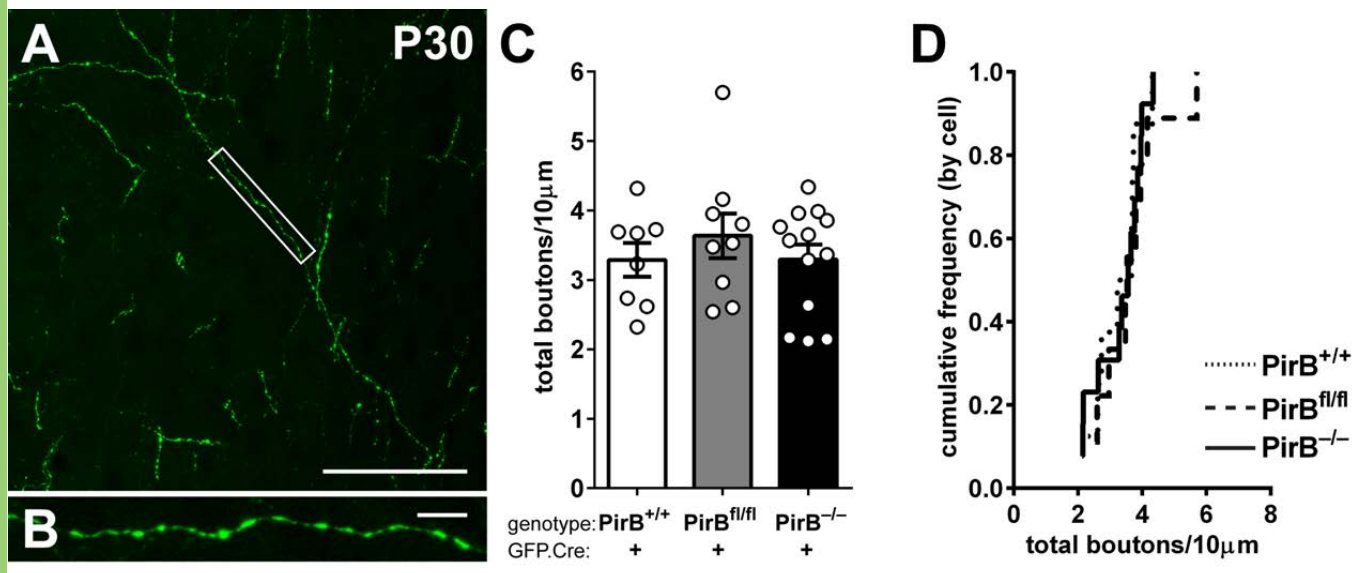

FIGURE 6